Published in final edited form as:
IEEE ASME Trans Mechatron. 2024 June ; 29(3): 1714–1725. doi:10.1109/tmech.2023.3329296.

Modeling and Control of an MR-Safe Pneumatic Radial Inflow Motor and Encoder (PRIME)

Anthony L. Gunderman [Student Member, IEEE],
Department of Biomedical Engineering, Georgia Institute of Technology/Emory, Atlanta, GA 30338 USA

Milad Azizkhani [Student Member, IEEE],
Department of Biomedical Engineering, Georgia Institute of Technology/Emory, Atlanta, GA 30338 USA

Saikat Sengupta,
Vanderbilt University Institute of Imaging Science, Vanderbilt University Medical Center, Nashville, TN 37232 USA

Kevin Cleary [Member, IEEE],
Children's National Hospital, Washington, DC 20010 USA

Yue Chen [Member, IEEE]
Department of Biomedical Engineering, Georgia Institute of Technology/Emory, Atlanta, GA 30338 USA

Abstract

Magnetic resonance (MR) conditional actuators and encoders are the key components for MR-guided robotic systems. In this article, we present the modeling and control of our MR-safe pneumatic radial inflow motor and encoder. A comprehensive model is developed that considers the primary dynamic elements of the system, including: 1) motor dynamics, 2) pneumatic transmission line dynamics, and 3) valve dynamics. After model validation, we present a simplified third order model that facilitates design of a first order sliding mode controller (TO-SMC). Finally, the motor hardware is tested in a 7T MRI. No image distortion or artifacts were observed. We posit the MR-safe motor and dynamic model will lower the entry barriers for researchers interested in MR-guided robots and promote wider adoption of MR-guided robotic systems.

Index Terms—

Control; magnetic resonance (MR) safe; modeling; pneumatic motor

---

Corresponding author: Yue Chen, Department of Biomedical Engineering, Georgia Institute of Technology/Emory, Atlanta, GA 30338 USA (yue.chen@bme.gatech.edu).

Recommended by Technical Editor W. Kim and Senior Editor S. Katsura.

This article has supplementary material provided by the authors and color versions of one or more figures available at https://doi.org/10.1109/TMECH.2023.3329296.

I. INTRODUCTION

MAGNETIC resonance (MR) guided robotic interventions have been extensively studied in the past several decades due to the intrinsic advantage of coupling precise motions with high-resolution image feedback [1]. These robotic systems are capable of accurately delivering therapeutic treatments and have been proposed for several clinical procedures, including thermal ablation [2], intracerebral hemorrhage removal [3], [4], tumor ablation [5], prostate and gynecological brachytherapy [6], [7], [8], lower back pain injections [9], needle-based surgical interventions [10], and many more clinical scenarios [1].

Despite the benefits of MRI, robotic development is impeded by the limitations imposed by the magnetic field, which restricts ferromagnetic materials within the five gauss line [11]. Consequently, common robotic actuators like direct-current (dc) motors are unsuitable for MR-guided interventions. Commercial piezoelectric motors (PM) have been suggested as an alternative, which operate by inducing strain in crystals through the piezoelectric effect [12]. Monfaredi et al. [13] developed an MR-guided robot for needle placement in arthrography using PMs (Piezo LEGS, Upsala, Sweden). Li et al. [14] developed a robot for MR-guided lower back pain injections using PMs (Piezo LEGS, PiezoMotor AB, Sweden, and USR60-S4N, Shinsei Corp., Japan) that operate a bead-driven gear-box. Although PMs are an off-the-shelf solution, the driving electric current can still impact image quality [15]. Thus, imaging typically does not take place during motor operation. These limitations have motivated the development of alternative actuation modalities, such as hydraulic and pneumatic actuators [12]. Although, hydraulic actuators pose operational concerns due to the use of an external liquid that risks leakage within the MRI room, the motive force for pneumatic systems is safe, clean, and readily available (compressed, sterile air is available in the MRI room).

MR-conditional pneumatic actuators can be categorized into three types: 1) deformation-based stepper actuators (DBSA), 2) non-DBSA (nDBSA), and 3) continuous-based actuators (CBA). DBSAs convert deformation into step-based motion using unique geometries [12]. For example, Comber et al. [16] and Musa et al. [17] developed bellows actuators, while Pfeil et al. [18] implemented an auxetic-based actuator, all designed for needle-based interventions. However, these devices are often large and tailored to specific applications. nDB-SAs employ novel mechanisms for step-based motion, such as meshing gear teeth adopted by the authors in [19], [20], and [21], cycloidal motion presented by Liang and Tse [22], and reciprocating pistons demonstrated by Farimani and Misra [23]. Unlike DBSAs, nDBSAs have an output shaft for general rotary motion. However, both approaches typically require short pneumatic transmission lines (PTL), which necessitates proper shielding of the valves to preserve image quality [24]. For a comprehensive review of MR-conditional actuators, see [12].

CBAs operate analogously to brushed dc motors. Mass flow rate of the air (similar to electrical current) is supplied by a compressor (similar to electrical potential) to a rotor, enabling continuous rotary actuation. However, dynamic analysis of these pneumatic systems is complex due to their intrinsic nonlinear behavior with many unknowns. Consequently, control algorithms are often developed without a model, necessitating intricate controller design. Some examples include fuzzy logic controllers [25], fuzzy sliding mode controllers [26], and neural networks [27]. A recent study presented a nonlinear state space controller for a turbine CBA, but the PTL dynamics were ignored [28]. Instead, the system controller used pressure transducers at the motor input with short PTLs, an impractical setup for MR-guided interventions.

A. Contributions and Prior Work

In prior work, we developed a turbine-based CBA [29] for MR-guided interventions [3], [4]. Although the motor in [29] was empirically characterized, the governing equations describing the motor dynamics were not investigated. In our recent study, we presented fabrication protocols, as well as a preliminary investigation into the motor steady-state response [30]. However, we did not investigate the complete system dynamics. This article introduces the dynamic modeling and control of our MR-safe pneumatic radial inflow motor and encoder (PRIME, see Fig. 1). Our contributions are as follows.

1. We developed a lumped dynamic model based on the continuity and differential energy equations that describe the dynamics of the motor, PTL, and valve. This enables PTL mass flow rate and pressure prediction in both space and time, as well as motor torque and response prediction.
2. Using the lumped dynamic model with an understanding of the PTL behavior, we develop a simplified model to facilitate a nonlinear control design that utilizes only motor position error feedback and enables system stability.

To our knowledge, this is the first comprehensive model and model-based dynamic control strategy for analyzing turbine CBAs for MRI with long PTLs. We believe the theoretical contributions, along with the open-source motor hardware design [30], are vital for advancing MR-safe robotics, promoting wider adoption of MR-guided robotic interventions.

The rest of this article is organized as follows. Section II discusses the derivation of the dynamic model. Section III presents the control framework. Section IV details the experiments and results. Finally, Section V concludes this article.

II. PRIME DYNAMIC MODEL

The system model (see Fig. 2 for the modeling framework) includes the dynamics of the motor (see Section II-A), PTL (see Sections II-B through Section II-D), and valve (see Section II-E). In this section, we detail the modeling methodology and potential uncertainties. This model considers the pneumatic fluid (herein, air) to be compressible, where density, pressure, and mass flow rate are functions of space and time. This section is divided as follows. Section II-A discusses the motor dynamics; Sections II-B and II-C derive the differential equations for the mass flow rate and pressure distribution through the system using the continuity equation. Section II-D derives the pressure loss of the air using the differential energy equation. Section II-E discusses the valve dynamics. Finally, Section II-F concludes the section with a discussion of the potential system uncertainties.

A. Motor Dynamics

The derivation of the motor dynamics starts by writing the change in the angular momentum of the air applied to the rotor

$$\mathbf{T} = \dot{\mathbf{H}} \tag{1}$$

where **T** is the total torque exerted on the rotor and $\dot{\mathbf{H}}$ is the time rate of change of the air's angular momentum. The torque exerted on the rotor can be written as

$$\mathbf{T} = \left[\mathbf{r} \times \mathbf{F}_s + \int \mathbf{r} \times \mathbf{g}\rho \; d\mathcal{V}_r + \mathbf{T}_l\right]\mathbf{k} + b\dot{\theta} + J\ddot{\theta} \tag{2}$$

where **r** is the vector from the rotor's axis of rotation **k** to the point of the applied force, $\mathbf{F}_s$ are the parasitic surface forces due to friction and pressure, **g** is the gravity vector, ρ is the air density, $\mathcal{V}_r$ is the rotor volume, $\mathbf{T}_l$ is an external load torque, b is the damping coefficient, J is the rotational inertia, and $\dot{\theta}$ and $\ddot{\theta}$ are the rotational velocity and acceleration of the rotor. $\dot{\mathbf{H}}$ can be written as [31]

$$\dot{\mathbf{H}} = \frac{d}{dt}[m\,\mathbf{r}\,\mathbf{u}]\,\mathbf{k} \tag{3}$$

where m and **u** are the mass and velocity of the air, respectively. To simplify the abovementioned expressions, we rely on the following widely-used assumptions for turbine analysis [31].

1. The body forces on the rotor due to gravity are symmetric and equal (i.e., $\int \mathbf{r} \times \mathbf{g}\,\rho\; d\mathcal{V}_r = 0$).
2. The load torque is significantly larger than the surface forces. In other words, $\mathbf{T}_l \gg \mathbf{r} \times \mathbf{F}_s, \therefore \mathbf{r} \times \mathbf{F}_s \cong 0$).

Rewriting (1) by substituting (2) and (3) and using the abovementioned assumptions, we solve for the angular acceleration as

$$\ddot{\theta} = \frac{1}{J}\left[\left[\frac{d}{dt}[m\mathbf{r}\;\mathbf{u}] - \mathbf{T}_l\right]\mathbf{k} - b\dot{\theta}\right]. \tag{4}$$

The first term is often written for turbines with one flow path as

$$\frac{d}{dt}[m\mathbf{r}\;\mathbf{u}]\mathbf{k} = -\dot{m}(r_2u_{2,t} - r_1u_{1,t}) \tag{5}$$

where $\dot{m}$ is the mass flow rate of the air leaving the nozzle and $r_1u_{1,t}$ and $r_2u_{2,t}$ are the products of the rotor radius and tangential velocity component of the air at the blade tip (subscript 1) and root (subscript 2) of the rotor, respectively (see Fig. 3). The tangential velocity at the blade tip can be written as

$$u_{1,t} = |\mathbf{u}_1| \cos(\gamma) \tag{6}$$

where $|\mathbf{u}_1|$ is the magnitude of the velocity of the air leaving the nozzle and γ is its angle of attack. Ideally, the tangential velocity of the air leaving the rotor at the blade root is zero (i.e., $u_{2,t} = 0$). However, swirling can occur (i.e., $u_{2,t} \neq 0$), reducing efficiency. This swirling effect will vary with rotor speed. To account for this phenomenon, we first write the magnitude of the velocity of air through a cross section as

$$|\mathbf{u}| = \frac{\dot{m}}{\rho A} \tag{7}$$

where A is the cross-sectional area of the flow. Using (7) (where the mass flow rate entering and exiting the rotor are equal) and assuming constant density across the rotor $\left(|\mathbf{u}_1|A_1 = |\mathbf{u}_2|A_2 = \frac{\dot{m}}{\rho}\right)$, the magnitude of the velocities can be related by

$$|\mathbf{u}_2| = \frac{A_1|\mathbf{u}_1|}{A_2} \tag{8}$$

where A_1 and A_2 are the cross-sectional areas of the flow at the nozzle and blade root, respectively. Given $|\mathbf{u}_2|$, we write its tangential component as a function of the efficiency η as

$$u_{2,t} = |\mathbf{u}_2|(1 - \eta) \tag{9}$$

where η is a function of rotational speed, written as

$$\eta = m \cdot \dot{\theta} + b$$

$$m = \frac{1}{\dot{\theta}_{\max,m}}(\eta_{\dot{\theta}} - \eta_{\tau}), \;\; b = \eta_{\tau} \tag{10}$$

where $\eta_{\dot{\theta}}$ and η_{τ} are the efficiencies at the maximum rotational speed and stall torque, respectively, and $\dot{\theta}_{\max,m}$ is the maximum measured rotational velocity of the rotor. The maximum ideal rotational velocity can be calculated as

$$\dot{\theta}_{\max} = \frac{u_{1,t}}{r_1}. \tag{11}$$

Thus, we evaluate $\eta_{\dot{\theta}}$ and η_τ as follows:

$$\eta_{\dot{\theta}} = \frac{\dot{\theta}_{\max,m}}{\dot{\theta}_{\max}} \tag{12}$$

$$\eta_\tau = \operatorname{argmin}_\eta\left[\dot{m}(r_2u_{2,t} - r_1u_{1,t}) + \tau_{\max,m}\right] \tag{13}$$

where $\tau_{\max,m}$ is the measured stall torque at the maximum steady-state mass flow rate defined by the system design parameters (i.e., supply pressure and pneumatic losses). The torque applied by our motor, which has two inlets (herein flow paths, which produce clockwise and counterclockwise rotation), can be written in terms of the mass flow rate as

$$\tau = \frac{|\dot{m}_{2,N+2}|\dot{m}_{2,N+2}}{\rho_{2,N+2}}\left(\frac{r_1}{A_1}\cos(\gamma) - \frac{r_2}{A_2}(1-\eta)\right)$$

$$-\frac{|\dot{m}_{4,N+2}|\dot{m}_{4,N+2}}{\rho_{4,N+2}}\left(\frac{r_1}{A_1}\cos(\gamma) - \frac{r_2}{A_2}(1-\eta)\right) \tag{14}$$

where τ is the actual torque applied to the motor due to the air, and $\dot{m}_{j,N+2}$ and $\rho_{j,N+2}$ are the mass flow rates and densities of the air, respectively, from the two different flow paths, $j = 2$ and $j = 4$, leaving their respective nozzles. The subscript $N+2$ corresponds to a node at the motor nozzle (as shown in Fig. 2); the derivation for the mass flow rate and density of these nodes in the two possible flow paths will be discussed in Sections II-B and II-C. Finally, the rotor acceleration is written as

$$\ddot{\theta} = \frac{1}{J}\left[\tau - T_l - b\dot{\theta}\right] \tag{15}$$

where T_l is the load torque about the rotor's axis of rotation k.

B. Pneumatic Flow Analysis

Solving (14) and (15) requires the mass flow rate and density of the air at the rotor. This section derives the differential equations for the time and space dependent i) pressure and ii) mass flow rate. We start with the continuity equation of a control volume

$$\nabla \cdot \rho \mathbf{u} + \frac{\partial \rho}{\partial t} = 0 \tag{16}$$

where ρ and $\mathbf{u}$ are the density and velocity of the fluid, respectively, within the control volume. Assuming the flow is collinear with the PTL center-line, which is reasonable due to the small PTL diameter, we rewrite (16) as

$$\frac{\partial \rho u_x}{\partial x} + \frac{\partial \rho}{\partial t} = 0 \tag{17}$$

where u_x is the velocity of the air with respect to position x along the PTL. Rewriting (17) in its expanded form, we obtain

$$\frac{\partial \rho}{\partial t} + u_x \frac{\partial \rho}{\partial x} + \rho \frac{\partial u_x}{\partial x} = 0. \tag{18}$$

Using the relationship defined by the total derivative

$$\frac{D\rho}{Dt} = \frac{d\rho}{dt} = \frac{\partial \rho}{\partial t} + u_x \frac{\partial \rho}{\partial x}. \tag{19}$$

We can rewrite (18) as

$$\frac{d\rho}{dt} + \rho \frac{\partial u_x}{\partial x} = 0 \tag{20}$$

Using (7) and the Ideal Gas Law, written as

$$P\cancel{V} = mRT \tag{21}$$

where P, $\cancel{V}$, m, R, and T are the pressure, volume, mass, specific gas constant (air: 287.05 $[\mathrm{J/(kg \cdot K)}]$), and temperature, respectively, within the control volume $\cancel{V}$, (20) can be rewritten to solve for the time rate of change of pressure as

$$\frac{dP}{dt} = -\frac{RT}{A}\frac{\partial \dot{m}}{\partial x} - \frac{\rho \dot{m} RT}{A}\frac{\partial\left(\frac{1}{\rho}\right)}{\partial x}. \tag{22}$$

Equation (22) is the first primary governing equation.

To obtain the time rate of change of the mass flow rate, we analyze the forces acting on the air in the control volume [32]

$$\rho A dx \frac{du_x}{dt} = PA - A\left(P + \frac{\partial P}{\partial x}\right) - dP_{\text{loss}}A \tag{23}$$

where dP_{loss} is the pressure loss of the fluid across the control volume in the form of frictional and pneumatic losses. Note that dP_{loss} is affected by flow speed in a nonlinear manner and will be discussed in Section II-D. Using (7), (23) can be rewritten to solve for the time rate of change of mass flow rate as

$$\frac{d\dot{m}}{dt} = -A\frac{\partial P}{\partial x} - \rho\dot{m}\frac{d\left(\frac{1}{\rho}\right)}{dt} - A\frac{dP_{\text{loss}}}{dx}. \tag{24}$$

Equation (24) is the second primary governing equation. For PTLs, (22) and (24) must be evaluated in a lumped model. Section II-C will discuss this process.

C. Lumped Model of Section II-B

To apply (22) and (24), a lumped model is proposed. The pneumatic system is divided into two flow paths representing each valve outlet, labeled as 2 and 4 per 5–3 valve convention. Each flow path has $(N + 2)$ segments describing the dynamics from the valve outlet to the exhaust (see Fig. 2). This results in $2(N + 2) + 1$ nodes, with the final node representing the joining of the flow paths at the exhaust.

The pressure change in the ith node $(i \in [1, \ldots, N + 2,\ \text{Exit}])$ of the jth flow path $(j \in [2,\ 4])$ can be written using (22) as

$$\frac{dP_{j,i}}{dt} = -\frac{RT}{A_{j,i}}\frac{(\dot{m}_{j,i} - \dot{m}_{j,i-1})}{dx_{j,i}} \tag{25}$$

where $\dot{m}_{j,i-1}$ and $\dot{m}_{j,i}$ are the mass flow rates entering and leaving the node, respectively, $dx_{j,i}$ is the length of the node, $A_{j,i}$ is the cross-sectional area of the node, and $\frac{\partial\left(\frac{1}{\rho}\right)}{\partial x}$ from (22) is neglected as the density is constant across the node. Note that $A_{j,i}$ of the PTL (5233K52, McMaster, USA) is assumed constant. This is supported by a hoop strain analysis of the PTL [33], which has an outer and inner diameter of 6.35 mm and 3.175 mm, respectively, and a durometer of 65 A that corresponds to a modulus of elasticity of 4.43 MPa using the relationship in [34]. Subjecting the tube to a 0.62 MPa internal pressure (the maximum pressure in this study) results in a diameter change of only 0.0027%. This suggests that tube deformation due to internal pressure will not impact the PTL dynamics. The change in mass flow rate in the *i*th node of the *j*th flow path can be written using (24) as

$$\frac{d\dot{m}_{j,i}}{dt} = A_{j,i}\frac{P_{j,i-1} - P_{j,i}}{dx_{j,i}} - A_{j,i}\frac{dP_{\text{loss},j,i}}{dx_{j,i}} \tag{26}$$

where $P_{j,i-1}$ and $P_{j,i}$ are the pressures driving the mass flow rate, $dP_{\text{loss},j,i}$ is the pressure loss across the node, and $\frac{d\left(\frac{1}{\rho}\right)}{dt}$ from (24) is often neglected [32]. These differential equations are subject to the following boundary differential equations at the inlet of the tube $(i = 1)$ and the exhaust of the motor (i = Exit):

$$\frac{dP_{2,1}}{dt} = \begin{cases} -\frac{RT}{A_{2,1}}\frac{\left(|\dot{m}_v| - \dot{m}_{2,1}\right)}{dx_{2,1}} & \dot{m}_v > 0 \\ -\frac{RT}{A_{2,1}}\frac{\left(-\dot{m}_{2,1}\right)}{dx_{2,1}} & \dot{m}_v \le 0 \end{cases} \tag{27}$$

$$\frac{dP_{4,1}}{dt} = \begin{cases} -\frac{RT}{A_{4,1}}\frac{\left(|\dot{m}_v| - \dot{m}_{4,1}\right)}{dx_{4,1}} & \dot{m}_v < 0 \\ -\frac{RT}{A_{4,1}}\frac{\left(-\dot{m}_{4,1}\right)}{dx_{4,1}} & \dot{m}_v \ge 0 \end{cases} \tag{28}$$

$$\frac{dP_{\text{Exit}}}{dt} = -\frac{RT}{A_{\text{Exit}}}\frac{\left(\left(\dot{m}_{2,N+2} + \dot{m}_{4,N+2}\right) - \dot{m}_{\text{Exit}}\right)}{dx_{\text{Exit}}} \tag{29}$$

$$\frac{d\dot{m}_{\text{Exit}}}{dt} = A_{\text{Exit}}\frac{P_{\text{Exit}} - P_{\text{Atm}}}{dx_{\text{Exit}}} - A_{\text{Exit}}\frac{dP_{\text{loss,Exit}}}{dx_{\text{Exit}}} \tag{30}$$

where $\dot{m}_v$ is the mass flow rate leaving the valve (see Section II-E), P_{Atm} is the atmospheric pressure, and $\dot{m}_{\text{Exit}}$ and P_{Exit} are the mass flow rate and pressure at the exhaust. The inequalities in (27) and (28) are based on the valve operation, which eliminates flow to one outlet when the other is open. By solving the $4(N + 2) + 2$ differential equations, $\dot{m}_{2,N+2}$, $\dot{m}_{4,N+2}$, $\rho_{2,N+2}$, and $\rho_{4,N+2}$ from (14) can be solved. Note that a discussion is still warranted on $dP_{\text{loss},j,i}$.

D. General Energy Equation Analysis of Pressure Loss

In this section, we provide a formulation for dP_{loss} in (26) and (30). We start with the general energy equation describing the energy of the air between two locations, written as

$$H_1 + \frac{mu_1^2}{2} + mgz_1 + Q_h = H_2 + \frac{mu_2^2}{2} + mgz_2 + W \tag{31}$$

where g is the acceleration constant of gravity, H and z are the enthalpy and height of the air, Q_h is external heat added to the air, and W is the work done by, or on, the air. Due to the low fluid speeds $(u < 100\frac{m}{s})$ we assume the process is adiabatic. Thus, $Q_h = 0$ and ΔH can be written as

$$\Delta H = H_2 - H_1 = \int_1^2 \not{V}\, dP\,. \tag{32}$$

Substituting (32) into (31) and dividing by the mass, we obtain

$$\int_1^2 \frac{1}{\rho} dP = w + \frac{1}{2}\left(u_2^2 - u_1^2\right) + g\left(z_2 - z_1\right) \tag{33}$$

where w is work per unit mass. Expressing (33) in differential form, we obtain

$$dP_{\text{loss}} = \rho\left(dw_F + dw_T + udu + gdz\right) \tag{34}$$

where dw_F is the pressure loss due to PTL friction and local resistances and dw_T is the pressure loss due to differential work performed by the air. Often, udu is neglected and gdz is zero due to the negligible height change. dw_F is written as

$$dw_F = \left(f\frac{dx}{D_E} + K\right)\frac{u|u|}{2} \tag{35}$$

where f is the dimensionless friction factor obtained using Churchill's explicit formulation [35], K is the dimensionless local resistance coefficient [36], dx is the differential length, and D_E is the effective diameter of the cross section. The differential work extracted from the turbine is written as

$$dw_T = \tau\dot{\theta}\,. \tag{36}$$

Using (34) through (36), the pressure loss in each node of flow path j for all nodes except $i = N + 2$ (rotor) can be written as

$$dP_{\text{loss}, j, i} = \left(f \frac{dx_{j, i}}{D_{E, j, i}} + K_{j, i}\right) \frac{\dot{m}_{j, i}\left|\dot{m}_{j, i}\right|}{2\rho_{j, i}A_{j, i}} \tag{37}$$

and for node $i = N + 2$ (rotor), we can write

$$dP_{\text{loss}, j, N + 2} = \tau\dot{\theta} . \tag{38}$$

Using (37) and (38), (26) and (30) can be evaluated. However, an expression for $\dot{m}_v$ is needed to complete the derivation.

E. Valve Dynamics

In our system, a proportional directional control valve is used (MPYE-5-1/8-LF-010-B, Festo, Germany). In this type of control valve, the spool position is proportional to the valve signal. However, it is critical to note flow rate is not proportional to spool position. Thus, the dynamics of the valve must be considered, which can be divided into two domains: 1) the air dynamics and 2) the mechanical spool dynamics.

The air dynamics of the control valve can be written as [32]

$$\dot{m}_v = \begin{cases} P_u C_s \rho_{\text{Atm}} \sqrt{1 - \left(\dfrac{\dfrac{P_d}{P_u} - b_s}{1 - b_s}\right)^2} & \text{for } \dfrac{P_d}{P_u} > b_s \\ P_u C_s \rho_{\text{Atm}} & \text{for } \dfrac{P_d}{P_u} \le b_s \end{cases} \tag{39}$$

where P_u is the pressure entering the valve (herein, $P_u = P_s$, where P_s is the supply pressure in Fig. 2), P_d is the pressure exiting the valve, and b_s is the critical pressure ratio. C_s is the sonic conductance due to spool position, which is linearly approximated with respect to spool position as

$$C_s = C \cdot \frac{d}{100} \tag{40}$$

where C is the sonic conductance defined by the manufacturer and d is the percent valve displacement, which is proportional to voltage (i.e., $10\ \text{V} \propto 100\%$ and $-10\ \text{V} \propto -100\%$). In this work, positive and negative valve displacement indicates flow through port 2 and port 4 of the valve, respectively. As a result, the P_d term changes based on spool position, written as

$$P_d = \begin{cases} P_{2,1} & C_s \geq 0 \\ P_{4,1} & C_s < 0. \end{cases} \tag{41}$$

This concludes the air dynamics of the valve as the exhaust ports on the valve are plugged.

The mechanics relating the spool position of the valve to the input signal is modeled assuming that the spring-loaded spool is a second order system [32]. We assume that the system is critically damped and define the natural frequency ω_n of the system using the manufacturer specified switching time. The switching time is defined as the time for the spool to displace from 0 to 100%. We choose to define the natural frequency of the system using the 5% settling time criterion, written as

$$\omega_n = \frac{3}{\zeta(0.95 t_s)} \tag{42}$$

where $\zeta = 1$ is the damping ratio and t_s is the switching time. This results in a natural frequency (760 rad/s) approximately equal to the critical frequency of the valve [37].

Using the second order system to find the spool position, the sonic conductance can be solved using (40). Substituting (40) into (39), $\dot{m}_v$ can be used to define the inputs into (27) and (28) to evaluate the lumped dynamic model described by (25)–(30). Solving the $4(N+2)+2$ differential equations, we are able to obtain the mass flow rates and density of the fluid at the rotor from (14) (i.e., $\dot{m}_{2,N+2}$, $\dot{m}_{4,N+2}$, $\rho_{2,N+2}$ and $\rho_{4,N+2}$), defining the motor dynamics in (15). This concludes the derivation of the full system dynamics.

F. System Model Uncertainties

The results of all pneumatic system models, both dynamic and steady-state, are subject to uncertainties. These uncertainties include variance due to tubing tolerances specified by the manufacturer, such as length and diameter, and local resistance loss assumptions [$K_{j,i}$ term in (37)]. In this section, we predict the overall anticipated uncertainty based on the relative uncertainty defined by the manufacturer tolerances.

Consider a simulation result R with J parameters X (i.e., $R(X_1, X_2, \ldots, X_J)$). Each parameter can be written as

$$X_i = X_{i0} \pm U_i \tag{43}$$

where X_{i0} is the nominal parameter value of the simulation and U_i is the uncertainty in the physical system. The effect of all the uncertainties on the results can be written as

$$U_R = \pm\sqrt{\sum_{i=1}^{J}\left(\frac{\partial R}{\partial X_i}U_i\right)^2} \tag{44}$$

where U_R is the total uncertainty in the result. The relative uncertainty can, thus, be written as

$$\frac{U_R}{R} = \pm\sqrt{\sum_{i=1}^{J}\left(\frac{\partial R}{\partial X_i}\frac{X_i}{R}\right)^2\left(\frac{U_i}{X_i}\right)^2} \tag{45}$$

where the first squared term can be thought of as the normalized sensitivity coefficients and the second squared term can be thought of as the relative uncertainty caused by each individual uncertainty. In this work, the i) mass flow rate and ii) torque output can be used to validate Sections II-A through Sections II-E in steady state.

The steady-state mass flow rate in the system is dependent on PTL length L, diameter D_E, loss coefficients K, and the pressure loss across the system. The total pressure loss across the system is known by $P_u - P_{\mathrm{Atm}}$. Thus, the uncertainties of the mass flow rate include $R_{\dot{m}}(L, D_E, K)$. The relative uncertainties are defined by each component's tolerance. The length of the PTL can be cut to a tolerance of 1.58 mm (0.16% for 1 m PTL and 0.02% for 10 m PTL), the diameter tolerance, as specified by the manufacturer, is 0.08 mm (2.52% of 3.175 mm ID tube), and the loss coefficient K of the system is often approximated as 10% of the sum of all coefficients [38]. Evaluating the partials and solving for the relative uncertainty, we obtain an overall relative uncertainty for the mass flow rate of ±10.58%. These anticipated errors are similar to other PTL models [39], [40]. Thus, the goal of this work is to provide a model that approximates mass flow rate with an error of ±10.58% (validating Sections II-B through Section II-D).

The resulting torque at a given speed in steady-state conditions is dependent only on the mass flow rate. The relative uncertainty of the mass flow rate is 10.58%. Evaluating the partial of torque to mass flow rate, we obtain a relative uncertainty in the torque of ± 21.17%. Thus, we aim to provide a model that approximates the torque with an error of ±21.17% in the steady-state condition (validating Sections II-A through Section II-E).

III. SIMPLIFIED MODEL AND MOTOR CONTROL

In the previous sections, a comprehensive lumped model was presented describing the system dynamics. However, the model uses a set of equations that are not suitable for control algorithm design. In this section, we propose a simplified dynamic model based on the lumped model and apply it to a model-based, robust nonlinear control framework.

A. Simplified Dynamic Model Derivation

To enable effective control of the proposed motor, several assumptions are made to produce a simplified model.

1) Motor Dynamics Assumptions:

1. The PTL is treated as if it has only one flow path, where the nozzle changes the flow direction based on the sign of $\dot{m}$. Thus, (14) can be written as

$$\tau = \frac{|\dot{m}|\ \dot{m}}{\rho}\left(\frac{r_1}{A_1}\cos(\gamma) - \frac{r_2}{A_2}(1-\eta)\right). \tag{46}$$

2. The rotor is small and the air jet stream travels a short distance, allowing the air stream area to remain constant. Thus, $A_1 = A_2 = A$ in (46), where A is the nozzle area.
3. The motor dynamics are of significant interest near the setpoint. Thus, control is crucial when the rotor is not near its terminal velocity. As such, $\eta = \eta_\tau$ in (46).
4. The PTL causes back-pressure and a significant lagging behavior. Due to this phenomenon, along with the switching behavior of the proposed controller, pressure is relatively constant at the rotor as the motor approaches the setpoint. Thus, the density in (46) can be approximated as constant. The lumped fluidic model is used to obtain ρ based on PTL length with the valve fully open [i.e., $\rho = \frac{P_{2,N+2}}{RT}$, when $d = 100\%$ in (40)].

2) PTL Dynamics:

5. The PTL dynamics can be approximated using e^{-sT} [41], where e here is the exponential constant, $T = \frac{L}{c}$ is the time delay, L is the PTL length, and c is the speed of sound (343 m/s). Since we are primarily interested in the lagging behavior, and our system is minimum phase, we approximate e^{-sT} using a first-order Taylor Series expansion to facilitate controller design, written as $e^{-sT} = \frac{1}{e^{sT}} \approx \frac{1}{(1+sT)}$.

3) Valve Dynamics:

6. Similar to assumption 4, P_d in (39) can be treated as constant. The lumped fluidic model is used to obtain P_d based on PTL length with the valve fully open [i.e., $P_d = P_{2,1}$, when $d = 100\%$ in (40)].
7. Due to the fast-operational speed of the valve, the mechanical dynamics of the valve can be ignored.

Using assumptions 1–4 and 6–7, we can write (46) as

$$\ddot{\theta} = [\alpha\dot{\theta} + \beta U],\ U = |\dot{m}|\ \dot{m}$$

$$\alpha = -\frac{b}{J}, \beta = \frac{\cos(\gamma)}{J\rho A}(r_1 - r_2(1 - \eta_\tau))\,. \tag{47}$$

Then, applying assumption 5 to (47), we can compensate for the PTL dynamics, writing the transfer function as

$$\frac{\theta(s)}{U(s)} = \frac{\beta}{s(s - \alpha)(1 + Ts)}\,. \tag{48}$$

B. Control Algorithm Derivation

Due to the motor's wide range of applications, our objective is to develop a control algorithm that ensures system robustness and accuracy. We achieve this goal by first using the second order simplified model in (47) to design a first-order sliding mode controller (SO-SMC). We further improve system control performance by compensating the PTL dynamics using the third order simplified model in (48) to design a sliding mode controller (TO-SMC).

The control signal in our system is the voltage signal that activates the valve (see Section II-E). Therefore, it is important to present the mapping from the designed control rule to the input voltage. Using (47), the flow rate can be calculated as

$$\dot{m} = sign(U)\sqrt{|U|}\,. \tag{49}$$

Using (49), the valve position, d, in (40) can be found based on (39) and assumption 6, which can then be mapped to voltage. The following sections will derive the control rule U.

1) Second Order System Sliding Mode Control:

By neglecting PTL dynamics when a short PTL is used, we can use (47). Thus, the SO-SMC can be defined as follows [42]:

$$S_2 = \dot{e} + 2\lambda_2 e + \lambda_2^2 \int e dt \tag{50}$$

where e is positional error (i.e., $e = \theta - \theta_d$), and λ is a positive constant value. The control rule can be defined as

$$U = \frac{1}{\beta}\left(\ddot{\theta}_d - 2\lambda_2\dot{e} - \lambda_2^2 e - \hat{\alpha}\dot{\theta} - k_2 \cdot sign(S_2)\right)$$

(51)

where k is a positive constant used to compensate unknown dynamics and $\hat{\alpha}$ is the approximation of α. By implementing (51) in (47), the closed-loop system can be described as follows:

$$\dot{S}_2 = (\alpha - \hat{\alpha})\ \dot{\theta} - k_2 \cdot sign(S_2)\,.$$

(52)

By considering the dynamics of the system and relying on our simplified model, the uncertainties of the system can be considered bounded, written as $|(\alpha - \hat{\alpha})\dot{\theta}| < F_2$. System stability is proved with the Lyapunov function, derived as [42]

$$V_2 = \frac{1}{2}S_2^2$$

(53)

where the differentiation of (53) can be written as

$$\dot{V}_2 = S_2\,\dot{S}_2 = S_2\ F_2 - k_2|S_2|.$$

(54)

Choosing $k_2 > F_2 + \eta_2$, where $\eta_2 > 0$, (54) can be rewritten as

$$\dot{V}_2 \leq -\eta_2|S_2|$$

(55)

which proves system stability.

2) Third Order System Sliding Mode Control: It has been shown that approximating the PTL dynamics will increase the system order. To improve system performance, we derive the TO-SMC based on (48), rewritten as

$$\dddot{\theta} = \frac{1}{T}\,[\alpha\dot{\theta} + (\alpha T - 1)\ddot{\theta} + \beta U]\,.$$

(56)

The sliding surface is defined as

$$S_3 = \ddot{e} + 3\lambda_3\dot{e} + 3\lambda_3^2 e + \lambda_3^3\int e dt\,.$$

(57)

We derive the control rule based on (48) as

$$U = \frac{T}{\beta}(\dddot{\theta}_d - 3\lambda_3\ddot{e} - 3\lambda_3^2\dot{e} - \lambda_3^3 e - \frac{\hat{\alpha}}{T}\dot{\theta} - \frac{(\hat{\alpha}T - 1)}{T}\ddot{\theta} - k \cdot sign\,(S_3))\,. \tag{58}$$

Using (58) in (56), the closed-loop system can be written as

$$\dot{S}_3 = \frac{(\alpha - \hat{\alpha})}{T}\dot{\theta} + (\alpha - \hat{\alpha})\ddot{\theta} - k_3 \cdot sign(S_3)\,. \tag{59}$$

Similar to the SO-SMC formulation, and relying on our model, we argue the system uncertainties are bounded, written as

$|\frac{(\alpha - \hat{\alpha})}{T}\dot{\theta} + (\alpha - \hat{\alpha})\ddot{\theta}| < F_3$. Writing the Lyapunov function as

$$V_3 = \frac{1}{2}S_3^2 \tag{60}$$

and choosing $k_3 > F_3 + \eta_3$, system stability is guaranteed by

$$\dot{V}_3 \leq -\eta_3|S_3|\,. \tag{61}$$

3) Proportional-Derivative (PD) Controller: An overdamped PD controller is used to highlight the superiority of our proposed SMC approaches. To avoid tracking issues and instability caused by the PTL dynamics, we exclude the integral action. The PD controller is implemented to facilitate tunability for different PTL lengths, written as

$$V = -G(K_p e + K_d\dot{e}) \tag{62}$$

where K_p is the proportional gain, K_d is the derivative gain, G is the output gain for ease of tuning, and V is the valve voltage.

IV. RESULTS AND DISCUSSIONS

A. Evaluation of Motor Modeling: Steady State

In this section, we confirm the evaluation of i) $\dot{m}_v$ using (25)–(39) and ii) τ and $\dot{\theta}$ using $\dot{m}_v$, (14), and (15) when the system is in steady state conditions for one flow path (i.e.,

$\frac{d\dot{m}_{j,i}}{dt} = \frac{d\dot{m}_{\text{Exit}}}{dt} = \frac{dP_{j,i}}{dt} = \frac{dP_{\text{Exit}}}{dt} = 0$ and $\dot{m}_{j,i} = \dot{m}_{\text{Exit}}$ and $\ddot{\theta} = 0$ for $j = 2$ and $i = 1, 2, \ldots, N + 2$, Exit and $N = 10$). The motor was coupled to an electromagnetic brake (B6–12-2, Placid, USA) to simulate a load torque (see supplementary material). P_u was varied from 0.34 to 0.62 MPa in 0.069 MPa increments. At each P_u, the load torque was increased from zero to the stall torque for a gear reduction of 100:1 and 500:1. Each configuration was tested with a 1 m and 10 m PTL (5233K52, McMaster, USA). For each configuration, the mass flow rate was measured by recording the duration required for the compressor tank pressure to drop from 0.79 MPa to 0.65 MPa while the pressure to the valve is regulated to P_u. There were 20 data points for mass flow rate and 20 torque and power curves.

The mass flow rate error, calculated as the absolute difference between the measured and model predicted (lumped model) mass flow rate, averaged 6.71%±3.81% across all experiments. This is below the 10.58% uncertainty bound discussed in Section II-F, confirming the validity of Sections II-B through Sections II-E. The torque error, calculated as the absolute difference between the measured and model predicted (lumped model) torque, averaged 9.82% ± 5.08% across all experiments. This is below the 21.17% potential uncertainty, confirming the validity of Sections II-A through Sections II-E. A comparison of the torque and power curve for a 500:1 gear reduction with a 10 m PTL [see Fig. 4(a)] and a 100:1 gear reduction with a 1 m PTL [see Fig. 4(b)] can be seen in Fig. 4. Note $\eta_\tau \cong 0.55$ and $\eta_\omega \cong 0.45$ for all configurations. This provides a reliable approach for motor optimization given operation requirements. The motor, prior to the gear reduction, achieved a maximum torque and rotational speed of 1.18 N·mm and 34500 r/min, respectively, for the 10 m PTL at 0.62 MPa.

B. Evaluation of Motor Modeling: Dynamic State

In this section, we validate the proposed lumped model [i.e., solve for θ using (14), (15), and (25)–(39)] and the simplified model [i.e., solve for θ using (48)] in an open-loop transient state. The experimental setup in Section IV-A was used, but without the electromagnetic brake. P_u was 0.55 MPa. A chirp signal with a frequency range of 0.1 Hz to 1 Hz over 10 s was applied to the valve [see Fig. 5(a)]. Model validation was performed using a 100:1 gear reduction with both a 1 m PTL and a 10 m PTL [see Fig. 5(b)]. For the 1 m PTL, the average percent position error was 3.2% ± 2.36% for the lumped model and 11.03% ± 4.23% for the simplified model. For the 10 m PTL, the average percent position error was 4.42% ± 2.72% for the lumped model and 9.51% ± 6.86% for the simplified model.

Fig. 5(c) presents the open-loop Bode plot for the 10 m PTL, highlighting the accuracy of the lumped model and the suitability of the simplified model for controller design. The absolute error of the magnitude and phase was calculated at each frequency. The magnitude error between the simplified model and experimental results remained below 2.14 dB, while the magnitude error between the lumped model and experimental results remained below 1.6 dB. Both the simplified and lumped models exhibited phase errors below 1° compared to the experimental results. It is worth noting that although the simplified model exhibited slightly higher error, this will be compensated for by the proposed SMC.

C. Motor Control Performance

The proposed controllers were evaluated under various system configurations. These include 1 m and 10 m PTL, as well unloaded and loaded motor conditions. In the loaded evaluations, a torque of 25 N·mm (~35% of the stall torque of the motor with a 100:1 gear reduction and 10 m PTL) was applied at the output shaft. Note that the stall torque of rotary PMs are typically < 80 N·mm [12]. Experiments were conducted for setpoint (see Table I) and sine-wave tracking (see Table II) using a Simulink xPC target machine at a sampling frequency of 10 kHz. Examples of the performance can be found in the supplementary material. The errors presented in Tables I and II represent the mean and standard deviation of the L_1 norm of the error data points. Additionally, the number of occurrences of 0° error during setpoint tracking is presented in Table I. Motor rotation was measured using the manufactured rotary encoder [30]. Speed is numerically differentiated and filtered from encoder feedback and acceleration is numerically differentiated and filtered from speed. The differentiation and filtering are performed using a transfer function in Simulink, written as $(\frac{30s}{s+30})$.

1) Controller Implementation for Setpoint Tracking: Setpoint tracking was performed for five sequential setpoints (360°, −360°, 720°, −720°, and 1080°), repeated seven times to obtain statistically significant results (35 data points). The results can be seen in Table I, and the real-time performance can be found in the supplementary material.

For the simplest control scenario, which consisted of a 1 m PTL and no external load, the SO-SMC and TO-SMC present a high accuracy with mean L_1 norm error below 1°, while the PD controller exhibited errors over 20 times larger than the SMCs (see Table I). Following the unloaded case, a 25 N·mm load was applied to the output shaft. The TO-SMC and SO-SMC maintained their performance with the same control parameters, while the PD control output required an adjustment by a factor of 2 to obtain a similar response to the unloaded case.

Control performance was then evaluated with a 10 m PTL. Note that long PTLs preclude the use of large gains, as this can induce system instability due to the slow system response. Similar to the prior experiment, the controllers were first evaluated without any load. The TO-SMC resulted in the best accuracy, with a mean L_1 norm error < 3°. Both the TO-SMC and SO-SMC outperformed the PD control scheme. The system was then evaluated with a 25 N·mm load added to the output shaft. Again, the TO-SMC provided the best system performance. All results can be seen in Table I.

The proposed SMCs outperformed the PD controller, demonstrating their effectiveness. Note that the SMCs only require a change in λ during implementation for different operation scenarios, showcasing their robustness and generalizability, and the efficacy of the simplified motor model. Furthermore, the proposed TO-SMC exhibited a reduced mean and standard deviation error, and a higher number of 0° error occurrences in all tested scenarios, emphasizing the significance of compensating for the PTL dynamics.

2) Controller Implementation for Trajectory Tracking: Trajectory tracking was evaluated for 35 cycles for a sine-wave with an amplitude and frequency of 360° and 1 rad/s, respectively, emulating dynamic targeting scenarios, such as cardiac ablation [43] or liver interventions [17], [44]. These tracking experiments introduce additional complexities as they require compensation of dead zones introduced by the plastic gearbox and PTL length during continuous rotation. The results are summarized in Table II, and controller performance can be visualized in the supplementary material.

For the 1 m PTL configuration, both SMC's outperformed the PD controller. The performance of the SO-SMC and TO-SMC are comparable due to the negligible PTL dynamics ($T \cong 0.002\ \mathrm{s}$). However, with the 10 m PTL and the corresponding noticeable PTL dynamics ($T \cong 0.29\ \mathrm{s}$), the TO-SMC demonstrated a superior response, as highlighted in the supplementary material, emphasizing the effectiveness of the higher order simplified model for improving performance.

The controllers were then evaluated with 25 N·mm load applied to the motor output shaft. Using the 1 m PTL, the TO-SMC and SO-SMC presented smooth tracking capability while the PD controller exhibited an ON–OFF behavior. In the 10 m PTL loaded scenario, which can be considered as the most challenging, the TO-SMC presented the best accuracy due to its ability to compensate the PTL dynamics.

3) Disturbance Rejection of TO-SMC: Disturbance rejection was evaluated for the proposed controller (TO-SMC) using the configuration with a 10 m PTL and 100:1 gear reduction. An initial setpoint of 360° was prescribed. External disturbances were applied to the motor in different directions (see supplementary material). The motor was disturbed 25 times, providing a mean L_1 norm error of 5.26° ± 3.61°. However, as shown in our prior applications, the motor is typically coupled with a translational lead-screw, which further reduces the output error and speed and increases the torque [4], [45].

4) Repeatability and Reliability of TO-SMC: To evaluate the long-term reliability of the system, the motor was actuated for 1000 of the sine-wave cycles discussed in the previous subsection. This testing occurred after the experimental results presented in the prior sections and was followed by a 3-month holding period. Subsequently, the system was used to perform setpoint and sine-wave tracking with a 10 m PTL. No significant deviations in performance or accuracy were observed. For example, Fig. 6 depicts the sine-wave tracking results for the 10 m PTL with no load.

5) Application Example of TO-SMC: In a final system evaluation, the motor was used to control the trajectory of a translational lead-screw supporting a 4.5 kg mass (see experimental setup in the supplemental material). The translational lead-screw is a part of our ongoing work on robot-assisted shim coil positioning [46]. The motor used a 10 m PTL with a 100:1 gear reduction. The desired trajectory was a sine-wave with an amplitude and frequency of 20 mm and 0.25 rad/s. The motor tracking was repeated twice, as shown in Fig. 7. No significant deviation was observed between experiments, and the error remained below 1 mm after the initial acceleration. The mean L_1 norm error was 0.39 ± 0.18 mm.

D. MRI-Compliance

An imaging experiment was performed in a 7 Tesla scanner, as shown in Fig. 8(a) (Bruker Biospin Avance III HD) to validate the MR-compliance of PRIME attached to a linear rail made of plastic and carbon fiber components. Two-dimensional spoiled gradient-echo imaging (FOV: 96×96×1 mm^3, 0.5×0.5 mm^2 resolution, TR/TE = 50/2 ms) was performed on a spherical water phantom 3 cm from the motor and 1 cm above the carbon fiber linear rails. The experiment compared the signal-to-noise ratio (SNR) in three conditions: 1) absence of the robotic assembly, 2) presence of the robotic assembly in the scanner and turned off, and 3) operation of the robotic assembly inside the scanner [see Fig. 8(b)]. The SNR is evaluated in a 30×30 region of interest (ROI) as $\mathrm{SNR} = \frac{\mu_1}{\sigma_2}$, where μ_1 is the mean signal and σ_2 is the standard deviation of the ROI in the noise background of the image. There was less than 1% change in the SNR when the system was absent versus present and operating, validating the utility of the proposed system in high-strength MRI fields.

V. CONCLUSION

In this article, we present the modeling and control of PRIME, an MR-safe motor that is suitable for MR-guided robotic interventions. The primary contributions of this paper are twofold. 1) We present a comprehensive model using the continuity equation and the differential energy equation for analyzing the dynamics of an open pneumatic system. The model successfully predicted the system’s mass flow rate and the motor’s torque and rotational speed in the steady-state case, as well as position in the dynamic case. 2) Based on the lumped model, a simplified model is developed for design of a robust control scheme for setpoint tracking and sine-wave tracking given the PTL and motor parameters. It has been shown that by considering the PTL dynamics in the model and designing a TO-SMC, the controller can produce superior results compared to conventional control algorithms. We posit the proposed modeling and control framework will promote PRIME in the open-source community, which will eventually benefit other researchers, MRI scientists, physicians, and patients as a whole.

Supplementary Material

Refer to Web version on PubMed Central for supplementary material.

Acknowledgments

This work was supported in part by the National Institute of Neurological Disorders and Stroke under Award Number R01NS116148 and the National Institute of Biomedical Imaging and Bioengineering under Award Number R01EB034359 of the National Institutes of Health. The content is solely the responsibility of the authors and does not necessarily represent the official views of the National Institutes of Health.

Biographies

Anthony L. Gunderman (Student Member, IEEE) received the B.S. degree in mechanical engineering from the University of Arkansas, Fayetteville, AR, USA, in 2019. He is currently working toward the Ph.D. degree in robotics with the Georgia Institute of Technology, Atlanta, GA, USA.

His research interests include medical robotics, control, and medical devices.

Milad Azizkhani (Student Member, IEEE) received the B.S. degree in mechanical engineering from Bu-Ali Sina University, Hamedan, Iran, in 2017 and the M.S. degree in mechatronics engineering from Amirkabir University of Technology-Tehran Polytechnic, Tehran, Iran, in 2020. He is currently working toward the Ph.D. degree in robotics with the Georgia Institute of Technology, Atlanta, GA, USA.

His research interests include medical robotics, control, and soft robotics.

Saikat Sengupta received the M.S. degree in biomedical engineering from the University of Memphis, Memphis, TN, USA, in 2002, and the Ph.D. degree in biomedical engineering from Vanderbilt University, Nashville, TN, USA, in 2010.

He completed a Postdoctoral Fellowship with Vanderbilt University Institute of Imaging Science and became faculty as Research Assistant Professor in 2015. He currently develops motion and field inhomogeneity robust methods for high field structural and functional MRI.

Kevin Cleary (Member, IEEE) received the B.S. and M.S. degrees from Duke University, Durham, NC, USA, and the Ph.D. degree from the University of Texas, Austin, TX, USA, all in mechanical engineering.

He was an NSF-sponsored Postdoctoral Researcher with the Mechanical Engineering Laboratory, Tsukuba, Japan. He is currently the Technical Director of the Bioengineering Initiative, Sheikh Zayed Institute for Pediatric Surgical Innovation, Children's National Medical Center, Washington, DC, USA. He leads a research team developing technology to improve pediatric surgery, including robotics, navigation, and image fusion.

Yue Chen (Member, IEEE) received the B.S. degree in vehicle engineering from Hunan University, Hunan, China, in 2010, the M.Phil. degree from Hong Kong Polytechnic University, Hong Kong, in 2013, and the Ph.D. degree from Vanderbilt University, Nashville, TN, USA, in 2018, both in mechanical engineering.

Since 2021 Fall, he has been an Assistant Professor with the Biomedical Engineering Department, Georgia Institute of Technology/Emory University, Atlanta, GA, USA. His current research interests include medical robotics and soft robots.

REFERENCES

[1]. Su H et al. , "State of the art and future opportunities in MRI-guided robot-assisted surgery and interventions," Proc. IEEE, vol. 110, no. 7, pp. 968–992, Jul. 2022, doi: 10.1109/Jproc.2022.3169146.

[2]. Chen Y et al., "Treating epilepsy via thermal ablation: Initial experiments with an MRI-guided concentric tube robot," in Proc. Des. Med. Devices Conf., Minneapolis, Minnesota, USA, Apr. 10–13, 2017, Paper V001T02A002, doi: 10.1115/DMD2017-3408.

[3]. Chen Y, Godage I, Sengupta S, Liu C, Weaver K, and Barth E, "MR-conditional steerable needle robot for intracerebral hemorrhage removal," Int. J. Comput. Assist. Radiol. Surg, vol. 14, no. 1, pp. 105–115, Jan. 2019, doi: 10.1007/s11548-018-1854-z. [PubMed: 30173334]

[4]. Gunderman A et al. , "Non-metallic MR-guided concentric tube robot for intracerebral hemorrhage evacuation," IEEE Trans. Biomed. Eng, vol. 70, no. 10, pp. 2895–2904, Oct. 2023. [PubMed: 37074885]

[5]. Franco E, Brujic D, Rea M, Gedroyc WM, and Ristic M, "Needle-guiding robot for laser ablation of liver tumors under MRI guidance," IEEE-ASME Trans. Mechatron, vol. 21, no. 2, pp. 931–944, Apr. 2016, doi: 10.1109/Tmech.2015.2476556.

[6]. Chen Y et al. , "Design and fabrication of MR-tracked metallic stylet for gynecologic brachytherapy," IEEE/ASME Trans. Mechatron, vol. 21, no. 2, pp. 956–962, Apr. 2016. [PubMed: 28989272]

[7]. Gunderman AL et al. , "MR-tracked deflectable stylet for gynecologic brachytherapy," IEEE/ASME Trans. Mechatron, vol. 27, no. 1, pp. 407–417, Feb. 2022. [PubMed: 35185321]

[8]. Gunderman AL et al. , "MR-guided tissue puncture with on-line imaging for high resolution theranostics," in Proc. Int. Symp. Med. Robot, 2020, pp. 57–61.

[9]. Li G et al. , "Body-mounted robotic assistant for MRI-guided low back pain injection," Int. J. Comput. Assist. Radiol. Surg, vol. 15, no. 2, pp. 321–331, Feb. 2020, doi: 10.1007/s11548-019-02080-3. [PubMed: 31625021]

[10]. Musa M, Sengupta S, and Chen Y, "Design of a 6-DoF parallel robotic platform for MRI applications," J. Med. Robot. Res, vol. 7, Jun. 2022, Art. no. 2241005, doi: 10.1142/S2424905X22410057.

[11]. FDA, "Establishing safety and compatibility of passive implants in the magnetic resonance (MR) environment," 2014.

[12]. Xiao QY, Monfaredi R, Musa M, Cleary K, and Chen Y, "MR-conditional actuations: A review," Ann. Biomed. Eng, vol. 48, no. 12, pp. 2707–2733, Dec. 2020, doi: 10.1007/s10439-020-02597-8. [PubMed: 32856179]

[13]. Monfaredi R et al. , "A prototype body-mounted MRI-compatible robot for needle guidance in shoulder arthrography," in Proc. IEEE 5th RAS/EMBS Int. Conf. Biomed. Robot. Biomechatronics, 2014, pp. 40–45, doi: 10.1109/BIOROB.2014.6913749.

[14]. Li G et al. , "A fully actuated body-mounted robotic assistant for MRI-guided low back pain injection," in Proc. IEEE Int. Conf. Robot. Automat, 2020, pp. 5495–5501.

[15]. Wendt O, Oellinger J, Luth TC, Felix R, and Boenick U, "The effects of the use of piezoelectric motors in a 1.5-Tesla high-field magnetic resonance imaging system (MRI)," Biomed. Tech, vol. 45, no. 1/2, pp. 20–25, Jan./Feb. 2000, doi: 10.1515/bmte.2000.45.1-2.20.

[16]. Comber DB, Slightam JE, Gervasi VR, Neimat JS, and Barth EJ, "Design, additive manufacture, and control of a pneumatic, MR-compatible needle driver," IEEE Trans. Robot, vol. 32, no. 1, pp. 138–149, Feb. 2016, doi: 10.1109/TRO.2015.2504981. [PubMed: 31105476]

[17]. Musa MJ, Sharma K, Cleary K, and Chen Y, "Respiratory compensated robot for liver cancer treatment: Design, fabrication, and benchtop characterization," IEEE/ASME Trans. Mechatron, vol. 27, no. 1, pp. 268–279, Feb. 2022, doi: 10.1109/TMECH.2021.3062984.

[18]. Pfeil A et al., "A 3d-printed needle driver based on auxetic structure and inchworm kinematics," in Proc. ASME Int. Des. Eng. Tech. Conf. Comput. Inf. Eng. Conf.: 42nd Mechanisms and Robotics Conference, Quebec City, Quebec, Canada, Aug. 26–29, 2020, vol. 5A, pp. 57–61, Paper V05AT07A057.

[19]. Sajima H, Kamiuchi H, Kuwana K, Dohi T, and Masamune K, "MR-safe pneumatic rotation stepping actuator," J. Robot. Mechatron, vol. 24, no. 5, pp. 820–827, Oct. 2012, doi: 10.20965/jrm.2012.p0820.

[20]. Chen Y, Mershon CD, and Tse ZTH, "A 10-mm MR-conditional unidirectional pneumatic stepper motor," IEEE-ASME Trans. Mechatron, vol. 20, no. 2, pp. 782–788, Apr. 2015, doi: 10.1109/Tmech.2014.2305839. [PubMed: 25419104]

[21]. Stoianovici D, Patriciu A, Petrisor D, Mazilu D, and Kavoussi L, "A new type of motor: Pneumatic step motor," IEEE-ASME Trans. Mechatron, vol. 12, no. 1, pp. 98–106, Feb. 2007, doi: 10.1109/Tmech.2006.886258. [PubMed: 21528106]

[22]. Liang HP and Tse ZTH, "Cycloidal stepper motor: A systematic approach for designing a nonmagnetic rotary actuator," IEEE-ASME Trans. Mechatron, vol. 28, no. 1, pp. 71–79, Feb. 2023, doi: 10.1109/Tmech.2022.3197294.

[23]. Farimani FS and Misra S, "Introducing PneuAct: Parametrically-designed MRI-compatible pneumatic stepper actuator," in Proc. IEEE Int. Conf. Robot. Automat, 2018, pp. 200–205.

[24]. Sajima H, Sato I, Yamashita T, Dohi T, and Masamune K, "Two-DoF non-metal manipulator with pneumatic stepping actuators for needle puncturing inside open-type MRI," in Proc. World Automat. Congr, 2010, pp. 1–6.

[25]. Safak C, Topuz V, and Baba AF, "Pneumatic motor speed control by trajectory tracking fuzzy logic controller," Sadhana, vol. 35, no. 1, pp. 75–86, Feb. 2010, doi: 10.1007/s12046-010-0007-z.

[26]. Renn JC and Liao CM, "A study on the speed control performance of a servo-pneumatic motor and the application to pneumatic tools," Int. J. Adv. Manuf. Technol, vol. 23, no. 7/8, pp. 572–576, Apr. 2004, doi: 10.1007/s00170-003-1757-0.

[27]. Marumo R and Tokhi OM, "Modelling and control of a pneumatic motor using neural networks," in Proc. 1st Afr. Control Conf., Cape Town, South Africa, 2003.

[28]. Li M, "Design and stability analysis of a nonlinear controller for MRI-compatible pneumatic motors," Proc. Inst. Mech. Engineers, Part C: J. Mech. Eng. Sci, 2023, pp. 1–15, doi: 10.1177/09544062231171994.

[29]. Chen Y, Godage IS, Tse ZTH, Webster RJ, and Barth EJ, "Characterization and control of a pneumatic motor for MR-conditional robotic applications," IEEE-ASME Trans. Mechatron, vol. 22, no. 6, pp. 2780–2789, Dec. 2017, doi: 10.1109/Tmech.2017.2767906. [PubMed: 31105420]

[30]. Gunderman AL, Azizkhani M, Sengupta S, Cleary K, and Chen Y, "Open source MR-safe pneumatic radial inflow motor and encoder (PRIME): Design and manufacturing guidelines," in Proc. Int. Symp. Med. Robot, Apr. 2023, pp. 1–7.

[31]. Hill P and Peterson C, Mechanics and Thermodynamics of Propulsion, 2nd ed. London, U.K.: Pearson, 2014.

[32]. Beater P, Pneumatic Drives. Berlin, Germany: Springer, 2007.

[33]. Budynas RG and Nisbett JK, Shigley's Mechanical Engineering Design, 10th ed. New York, NY, USA: McGraw-Hill, 2015.

[34]. Gent AN, "On the relation between indentation hardness and young's modulus," Trans. Inst. Rubber Ind, vol. 34, pp. 46–57, 1958.

[35]. Churchill SW, "An explicit equation for friction factor in pipecomments," Ind. Eng. Chem. Fundam, vol. 19, no. 2, pp. 228–228, 1980.

[36]. Idelchik IE, Handbook of Hydraulic Resistance 3d ed., Boca Raton, FL, USA: CRC Press, 1993.

[37]. FESTO. "Proportional directional control valves MPYE," 2022. [Online]. Available: https://www.festo.com/media/pim/683/D15000100122683.PDF

[38]. Couvillion RJ, "MEEG 4483-thermal systems analysis/design," University of Arkansas, vol. Lecture 1–2, 2019.

[39]. Kern R, "Physical modelling of a long pneumatic transmission line: Models of successively decreasing complexity and their experimental validation," Math. Comput. Model. Dynamical, vol. 23, no. 5, pp. 536–553, 2017, doi: 10.1080/13873954.2017.1282880.

[40]. Kaminski Z, "A simplified lumped parameter model for pneumatic tubes," Math. Comput. Model. Dynamical, vol. 23, no. 5, pp. 523–535, 2017, doi: 10.1080/13873954.2017.1280512.

[41]. Yang B, Tan U-X, McMillan AB, Gullapalli R, and Desai JP, "Design and control of a 1-DOF MRI compatible pneumatically actuated robot with long transmission lines," IEEE ASME Trans. Mechatron, vol. 16, no. 6, pp. 1040–1048, Dec. 2011, doi: 10.1109/TMECH.2010.2071393. [PubMed: 22058649]

[42]. Slotine JJE and Li W, Applied Nonlinear Control. Englewood Cliffs, NJ, USA: Prentice-Hall, 1991, Art. no. 459.

[43]. Alipour A et al. , "MRI conditional actively tracked metallic electrophysiology catheters and guidewires with miniature tethered radio-frequency traps: Theory, design, and validation," IEEE Trans. Biomed. Eng, vol. 67, no. 6, pp. 1616–1627, Jun. 2020, doi: 10.1109/TBME.2019.2941460. [PubMed: 31535979]

[44]. Gunderman AL et al. , "Autonomous respiratory motion compensated robot for CT-guided abdominal radiofrequency ablations," IEEE Trans. Med. Robot. Bionics, vol. 5, no. 2, pp. 206–217, May 2023, doi: 10.1109/Tmrb.2023.3265718.

[45]. Chen Y, Howard J, Godage I, and Sengupta S, "Closed loop control of an MR-conditional robot with wireless tracking coil feedback," Ann. Biomed. Eng, vol. 47, no. 11, pp. 2322–2333, Nov. 2019, doi: 10.1007/s10439-019-02311-3. [PubMed: 31218486]

[46]. Hrovat M et al., "In-bore remotely-manipulated cantilevered cardiac shim system (CSS) corrects CMR artifacts due to implanted cardioverter defibrillators (ICDs): Phantom and swine validation," Soc. Cardiovascular Magnetic Resonance, London, U.K., 2024.

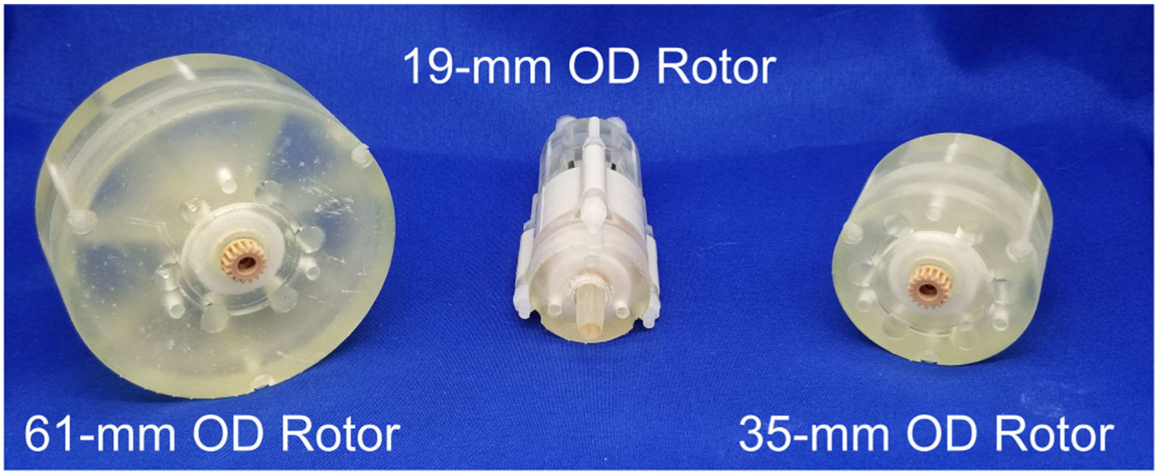

Fig. 1.
Proposed scalable motor design for MR-guided robotic interventions.

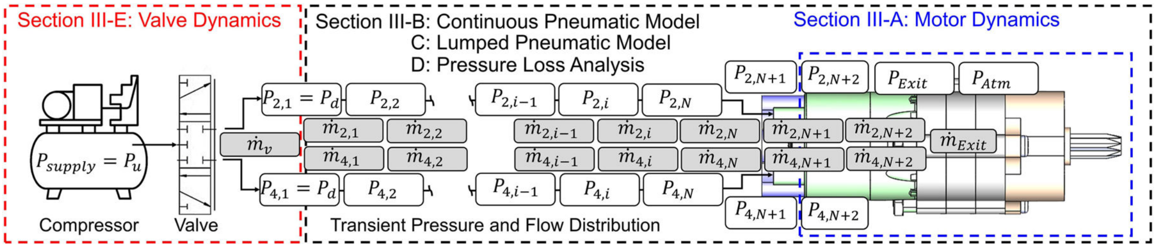

Fig. 2.

Modeling schematic of the system. This model includes the valve dynamics, PTL (lumped pneumatic model) dynamics, and the motor dynamics. Note that the valve has five ports. Port 1 is the inlet, port 2 and 4 are outlets, and port 3 and 5 are exhausts (which are plugged).

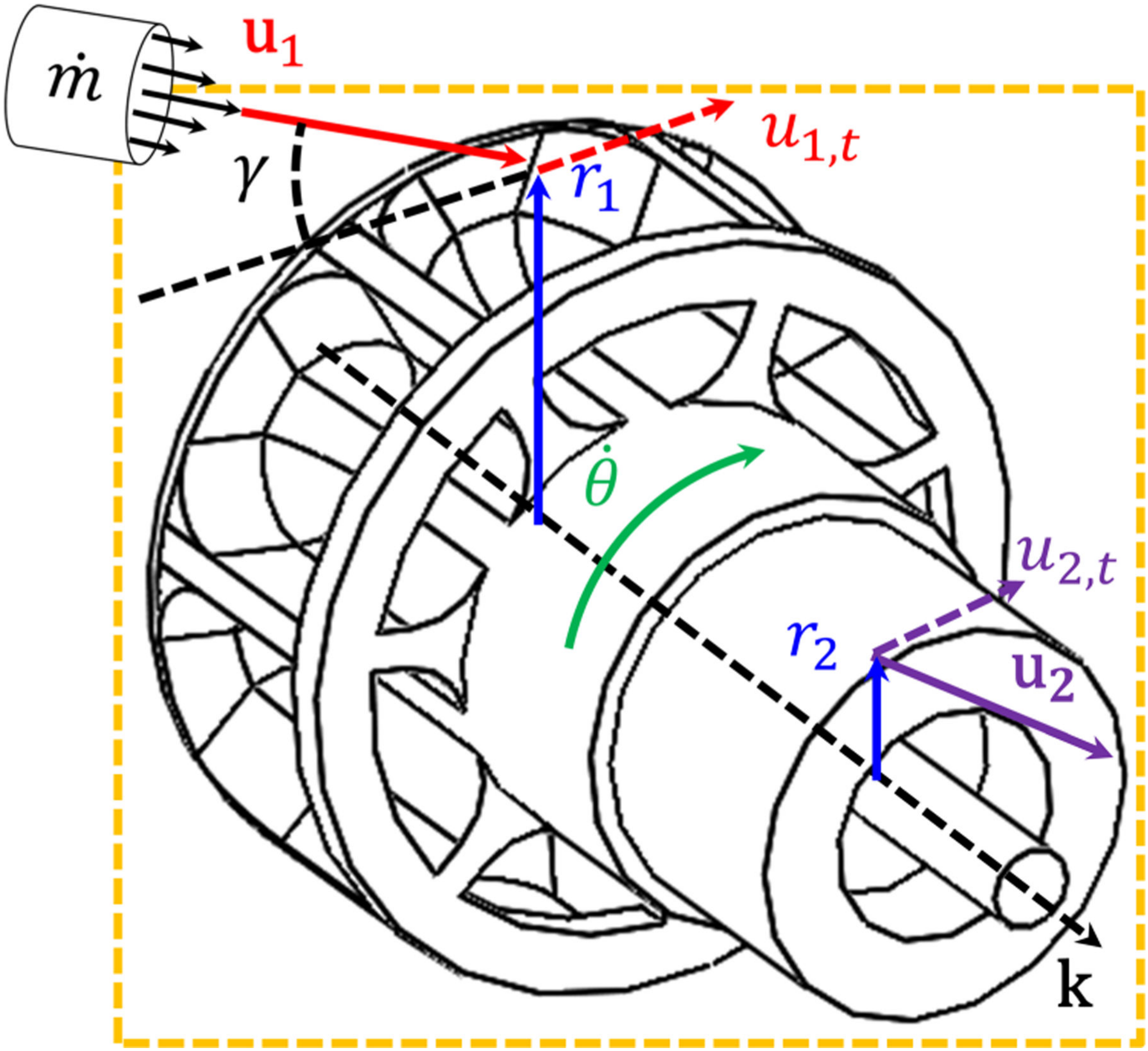

Fig. 3.

Rotor control volume (orange) and the absolute (solid arrow) and tangential (dashed arrow) velocity components of the air entering (red $\mathbf{u}_1$ at r_1) and leaving (purple $\mathbf{u}_2$ at r_2) are depicted.

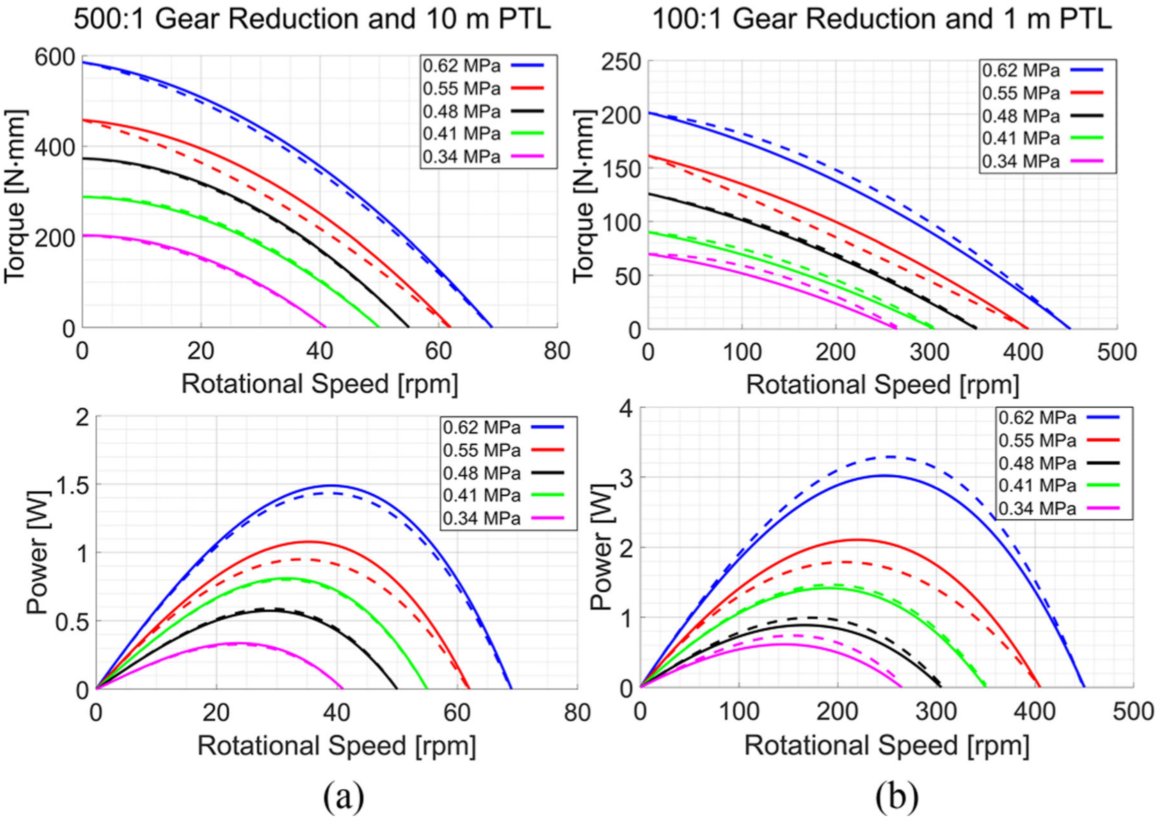

Fig. 4.

Motor model validations of the lumped model (solid line) compared to the experimental results (dashed lines). Torque and power curves for (a) 500:1 gear reduction with a 10 m PTL and (b) 100:1 gear reduction with a 1 m PTL.

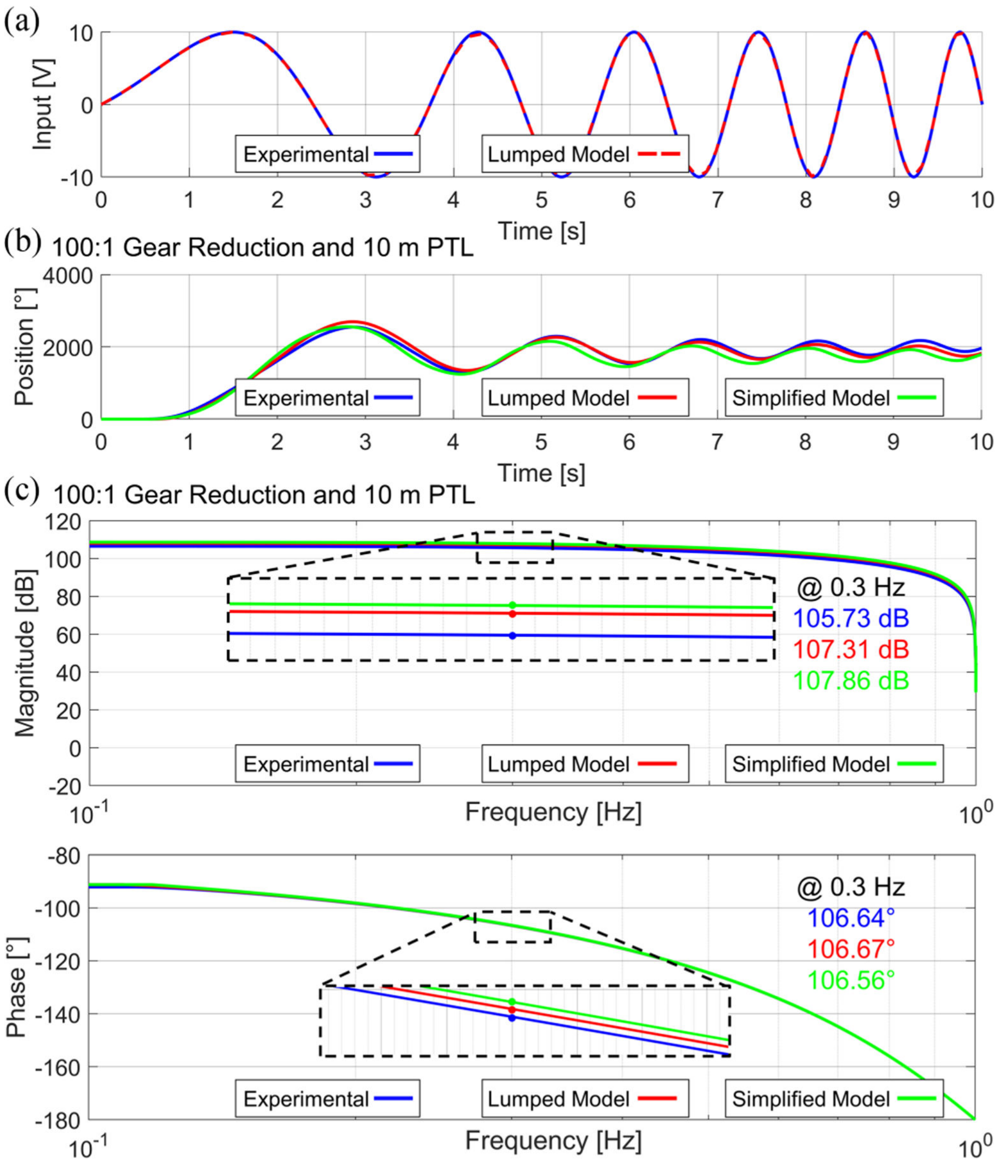

Fig. 5.

Chirp signal (a) was applied to the valve to compare the experimental data (blue) to the lumped model (red) and the simplified model (green) in a dynamic scenario using a (b) 10 m PTL with a 100:1 gearbox. The position for the output shaft is shown. The Bode plot for (b) is shown in (c).

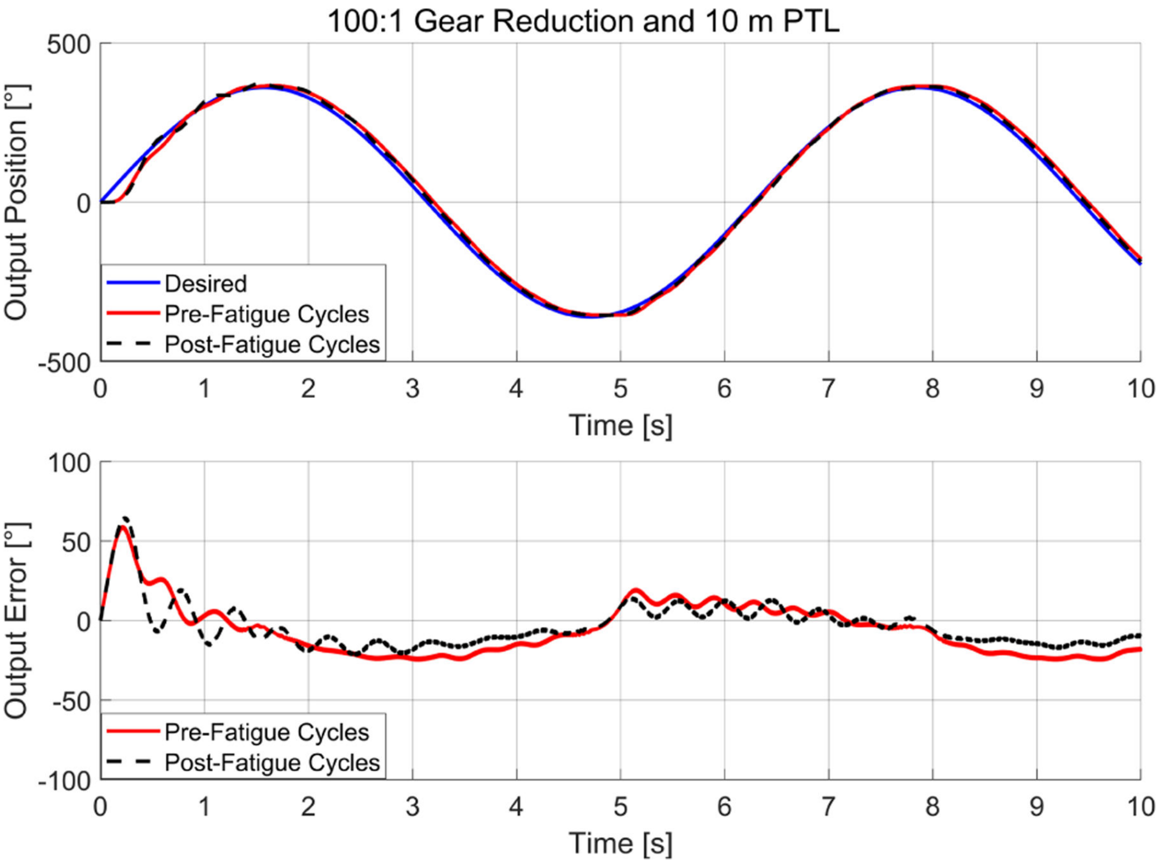

Fig. 6.

Sine-wave (blue) tracking performance using 10 m PTL with no load. Pre-fatigue data (red) is compared to post-fatigue data (black).

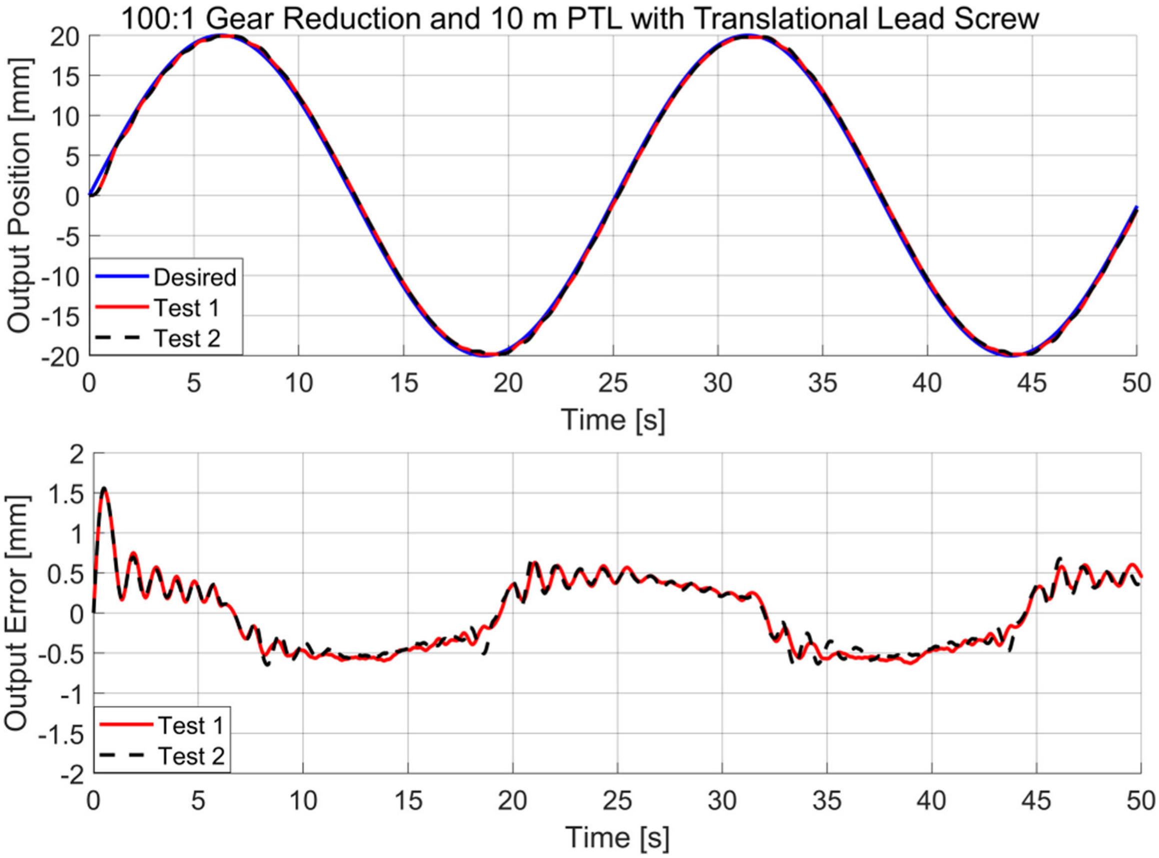

Fig. 7.

Sine-wave tracking performance using 10 m PTL with a 4.5 kg mass. Test 1 (red) can be seen compared to Test 2 (black) with respect to the desired trajectory (blue).

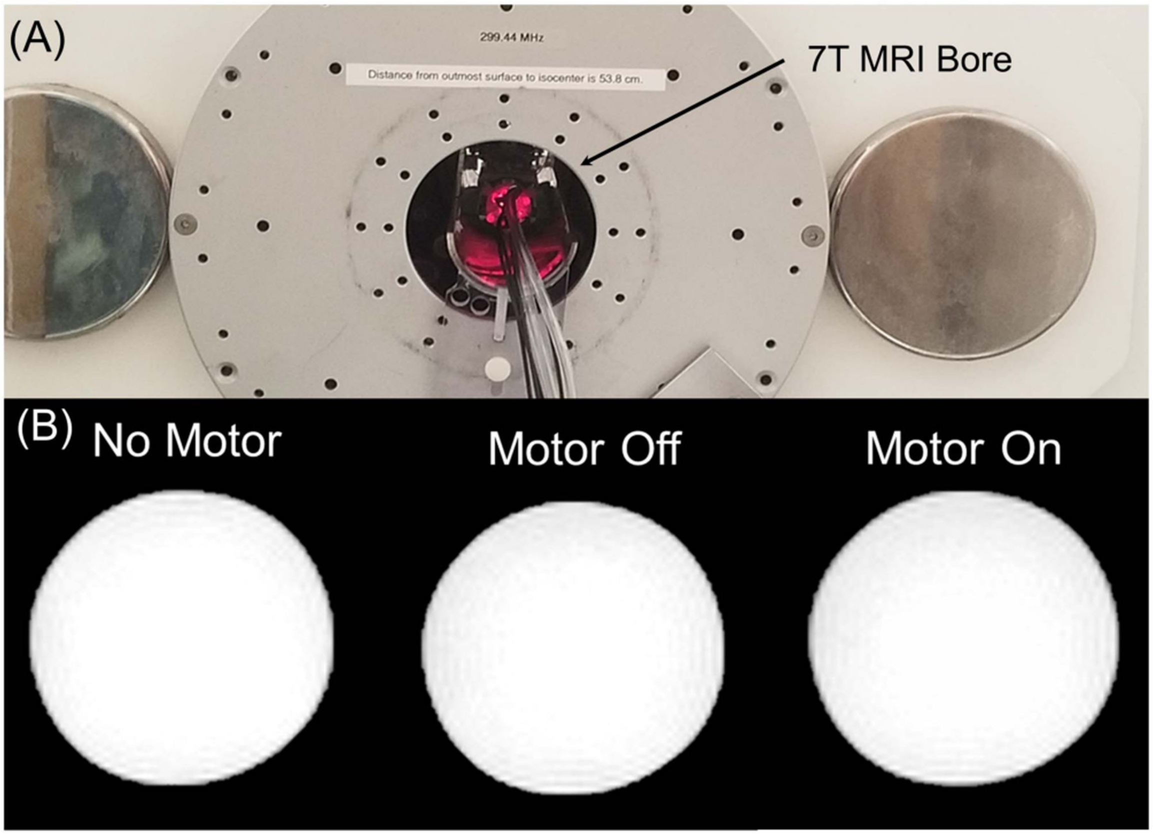

Fig. 8.

(a) 7T MRI bore with the robot system inside. (b) MRI images with different operation scenarios for comparative study.

TABLE I

SETPOINT TRACKING CONTROL PERFORMANCE

Mean and Standard Deviation of L_1 Norm of Error for Motor Setpoint Tracking Controller Performance

PTL[m]	Load [N·mm]	PD				SO-SMC				TO-SMC			
		Mean	Std	# of 0°	(K_p, K_d, G)	Mean	Std	# of 0°	(λ)	Mean	Std	# of 0°	(λ)
1	0	18.31°	3.66°	0	(0.025, 0.008, 3)	0.78°	0.58°	4	25	0.73°	0.56°	7	80
1	25	12.91°	4.79°	0	(0.025, 0.008, 6)	1.60°	1.04°	2	25	1.23°	0.91°	6	80
10	0	9.75°	5.49°	0	(0.025, 0.008, 1)	5.24°	3.01°	1	8	2.23°	0.53°	0	13
10	25	11.23°	4.12°	0	(0.025, 0.008, 3)	5.18°	3.19°	1	13	1.68°	1.21°	6	14

TABLE II

Dynamic Tracking Control Performance

Mean and Standard Deviation of L_1 Norm of Error for Motor Sine-Wave Tracking Controller Performance										
PTL[m]	Load [N·mm]	PD			SO-SMC			TO-SMC		
		Mean	Std	(K_p, K_d, G)	Mean	Std	(λ)	Mean	Std	(λ)
1	0	11.23°	4.86°	(0.025, 0.008, 3)	1.25°	1.03°	25	1.23°	0.92°	80
1	25	8.61°	3.86°	(0.025, 0.008, 6)	5.03°	1.50°	25	4.60°	1.18°	80
10	0	32.51°	15.85°	(0.025, 0.008, 1)	18.16°	17.11°	8	9.18°	8.10°	13
10	25	35.10°	26.51°	(0.025, 0.008, 3)	30.04°	25.09°	13	23.47°	11.78°	14